Atmospheric Environment 247 (2021) 118181

Contents lists available at ScienceDirect

Atmospheric Environment

journal homepage: http://www.elsevier.com/locate/atmosenv

Quantifying the impacts of anthropogenic and natural perturbations on gaseous elemental mercury (GEM) at a suburban site in eastern China using generalized additive models

Lei Zhang [a,b,*,1], Peisheng Zhou [a,1], Hui Zhong [a], Yu Zhao [a,b], Liang Dai [a], Qin'geng Wang [a], Mengxiao Xi [a], Yi Lu [a], Yutong Wang [a]

[a] School of the Environment, Nanjing University, 163 Xianlin Avenue, Nanjing, Jiangsu, 210023, China
[b] State Key Laboratory of Pollution Control and Resource Reuse, Nanjing University, 163 Xianlin Avenue, Nanjing, Jiangsu, 210023, China

HIGHLIGHTS

- Generalized additive models were utilized to quantify impacts of GEM origins.
- The impact of local anthropogenic emissions on GEM decreased in recent years.
- Natural perturbations became more and more essential to GEM in recent years.
- RH played a key role in GEM enhancement probably through Hg(II) reduction.

ARTICLE INFO

Keywords:
Gaseous elemental mercury (GEM)
Generalized additive model (GAM)
Anthropogenic emissions
Regional transport
Meteorological factors

ABSTRACT

Long-term observation of atmospheric mercury (Hg) concentration and observation-based statistical methods are important tools to quantify the impacts of anthropogenic and natural perturbation on the global atmospheric Hg reservoir. In this study, two campaigns were conducted at a suburban site in eastern China with continuous measurements of gaseous elemental mercury (GEM) during the periods of August 2014 to July 2015 (Campaign 1) and May 2018 to April 2019 (Campaign 2). The overall mean GEM concentrations were 3.77 ± 1.32 and 3.24 ± 1.26 ng m^{-3}, respectively. The potential source contribution function (PSCF) model based on backward trajectories were used to examine the variation of the potential source regions for GEM in different seasons. Generalized additive models (GAMs) were utilized in this study to quantify the impacts of local anthropogenic emissions, regional transport, and meteorological factors on the GEM concentration. Case studies with results from GAMs and observations of other air pollutants were conducted to provide more evidence for impacting mechanisms. The reduction of model residuals and the variation of contributions from direction and distance of air parcel transport imply the alleviation of local and regional anthropogenic Hg emissions from Campaign 1 to Campaign 2, respectively. The impact of relative humidity on GEM was crucial via the reduction of Hg(II) in droplets or on particles in the atmosphere. The impact of air stagnation on GEM was embodied mainly through the contribution of wind speed and partially by day of year (DOY) in winter. One DOY-controlled case also indicates the impacts of the 2015 El Niño event. With the decrease of anthropogenic emissions, the impacts of meteorological factors on GEM are getting more and more prominent. GAMs provide a promising tool for better understanding how anthropogenic and natural perturbations affect atmospheric Hg pollution.

1. Introduction

The pollution of mercury (Hg) has raised global concern for its persistency, neurotoxicity, long-range transport, and bioaccumulation (Ariya et al., 2015; Obrist et al., 2018). Totally 128 nations have signed the Minamata Convention on Mercury with 127 ratified, aiming to

* Corresponding author. State Key Laboratory of Pollution Control and Resource Reuse, Nanjing University, 163 Xianlin Avenue, Nanjing, Jiangsu, 210023, China.
E-mail address: lzhang12@nju.edu.cn (L. Zhang).
[1] These authors contributed equally to this work.

https://doi.org/10.1016/j.atmosenv.2020.118181
Received 31 July 2020; Received in revised form 6 December 2020; Accepted 29 December 2020
Available online 4 January 2021

protect human health and the environment from Hg emissions and releases (Selin et al., 2018; UN Environment, 2019). Hg in the atmosphere exists in three operationally defined forms: the gaseous elemental mercury (GEM), the gaseous oxidized mercury (GOM), and the particulate-bound mercury (PBM) (Gustin et al., 2015; Schroeder and Munthe, 1998). Due to its high volatility, low chemical reactivity, and low solubility in water, GEM has a long residence time in the atmosphere (0.5–1 yr) and plays an important role in global Hg cycling (Driscoll et al., 2013; Zhang et al., 2009). GOM and PBM, on the other hand, have a shorter lifetime (hours to weeks) and higher impacts on local ecosystems (Amos et al., 2012; Schroeder and Munthe, 1998).

Observation of atmospheric Hg concentration is crucial to understand the level of Hg pollution and its potential sources (Sprovieri et al., 2016). Results from long-term monitoring at global and regional background sites have shown significant decrease in atmospheric Hg concentration since the 1990s (Cole et al., 2013; Slemr et al., 2008, 2011; Weigelt et al., 2015; Weiss-Penzias et al., 2016). Zhang et al. (2016) reported the observed decreasing trends (1990s–2010s) of the GEM concentrations in North America ($-1.5 \pm 0.15\%$ yr^{-1}) and western Europe ($-2.1 \pm 0.46\%$ yr^{-1}) and attributed the decrease of GEM to the phase-out of Hg from commercial products and the co-benefit from SO_2 and NO_x emission control in coal-fired power utilities using the GEOS-Chem model. As a global hotspot region for Hg, East Asia has also started to exhibit decreasing trends in atmospheric Hg concentration in recent years. The GEM concentration at Mt. Changbai, a remote site in East Asia, increased from 2009 to 2013 and decreased from 2013 to 2015 (Fu et al., 2015). Nguyen et al. (2019) found a significant decreasing trend (-1.5% yr^{-1}) in nighttime GEM concentration at a remote site in East Asia from 2006 to 2016. Tang et al. (2018) observed a more aggressive decrease (-0.60 ± 0.08 ng m^{-3} yr^{-1}) in GEM concentration at a rural site in East Asia, more specifically eastern China, from 2014 to 2016, which was attributed mainly to the reduction of anthropogenic Hg emissions in China by the study of Liu et al. (2019) using GEOS-Chem.

Chemical transport models (CTMs), such as GEOS-Chem and CMAQ-Hg, have been utilized to simulate the variation trends of atmospheric Hg concentrations (Giang and Selin, 2016; Liu et al., 2019; Saiz-Lopez et al., 2018; Streets et al., 2019; Zhang et al., 2016; Zhu et al., 2015). However, atmospheric Hg processes in response to changes of emissions and meteorology have not been fully understood, which causes large uncertainties in CTM simulations (Ariya et al., 2015; Obrist et al., 2018; Pacyna et al., 2016; Zhang et al., 2017a). Recent studies on inter-annual Hg emission inventories (Liu et al., 2018; Wu et al., 2016, 2018; Zhang et al., 2015; Zhao et al., 2015) have shown mitigating or decreasing trends in the total anthropogenic Hg emission in China during the latest decade. The turning point was most likely between 2010 and 2015. This was not quite consistent with the study of global Hg emission inventories conducted by Streets et al. (2019). Meteorological impacts on atmospheric Hg have been qualitatively evaluated in many observational studies (Choi et al., 2013; Hong et al., 2016; Nair et al., 2012; Qin et al., 2019; Zhang et al., 2017b). However, the lack of quantitative studies leads to an incomplete understanding on the influence of meteorological factors on atmospheric Hg, making it become one of the main sources of uncertainties in the application of CTMs.

Besides CTMs, statistical models are also useful tools in quantifying the impacts of multiple factors on air quality. As a flexible statistical model, the generalized additive model (GAM) has been introduced to environmental studies for over 15 years (Aldrin and Haff, 2005; Camalier et al., 2007; Gong et al., 2017; Pearce et al., 2011; Rutterford et al., 2015). GAMs are data-driven and able to incorporate non-linear relationships in linking air pollution with numerical and categorical variables (Wood and Augustin, 2002). Camalier et al. (2007) used a GAM to quantify the impacts of meteorological factors on O_3 concentrations in eastern United States (US) urban areas and analyzed the spatial pattern of the impacts. Pearce et al. (2011) assessed the relationships between meteorological factors and air pollutants using GAMs in Melbourne, Australia, indicating local meteorology a relatively strong driver of air quality. Gong et al. (2017) extracted the influence of wildfires on O_3 anomalies in the western US by examining the residuals from GAM models. GAMs make no priori assumptions between predictors and dependent variables and are considered to reflect the nature of relationships, leading to the advantage of accuracy and the challenge of better reasoning (Gong et al., 2018; Rutterford et al., 2015).

With the mitigation of anthropogenic Hg emissions globally, particularly in China, natural perturbations (e.g., meteorological factors) tend to exert more and more profound impacts on atmospheric Hg behavior (Obrist et al., 2018). To quantify the impacts of both anthropogenic and natural perturbations on atmospheric Hg, this study applied GAM models to observations of GEM concentrations from two one-year-long campaigns at a suburban site in eastern China. Meteorological factors, backward trajectory features, and other relative parameters were considered as predictors in GAMs. The impact patterns of different predictors on GEM were identified in the two campaigns and hypotheses on the impact mechanisms were proposed. Evidences from Hg polluted episodes were provided to support these hypotheses. Overall, this study explored a new way of GAM application and found a promising tool in quantifying the contributions of anthropogenic Hg emissions and natural perturbations to GEM.

2. Methodology

2.1. Site description

The monitoring site (32°7′9″ N, 118°56′55″ E, 28 m above sea level) is located on the roof of the building for the School of the Environment, Nanjing University (NJU), which is to the northeast of downtown Nanjing as shown in Fig. 1. Nanjing is one of the core cities in the Yangtze River Delta (YRD) region, which is one of the most developed regions in China (Zhu et al., 2012). The petrochemical industry, iron and steel production, automobile manufacturing, electronics manufacturing, and power generation are the five pillar industries in Nanjing. The prevailing wind directions of Nanjing are northeast and southeast in cold and warm seasons, respectively. Therefore, the NJU site is generally upwind from downtown Nanjing and downwind from highly industrialized area in the YRD region (Ding et al., 2013).

2.2. Monitoring methods

Two campaigns with continuous measurements of the GEM concentration at the NJU site were conducted using the Tekran 2537X/1130/1135 system (Tekran Instrument Corperation, Canada) during the periods of August 2014 to July 2015 (Campaign 1) and May 2018 to April 2019 (Campaign 2). With GOM captured by the KCl-coated denuder in the 1130 module and PBM captured by the quartz filter in the 1135 module, GEM was analyzed every 5 min by 2537X using the cold vapor atomic fluorescence spectroscopy (CVAFS) method (Landis et al., 2002). The system was operated on a regular basis under the guidelines specified by the Atmospheric Mercury Network (AMNet) (http://nadp.slh.wisc.edu/AMNet/docs.aspx). The quartz filters, Teflon membranes, KCl-coated denuder and soda lime trap were changed every ten days, and the impactor frit was changed every five days. The 2537X analyzer was automatically calibrated every 25 h using the internal permeation source, and manually calibrated once during each campaign using the Tekran 2505 permeation source. Details on the quality assurance and quality control (QA/QC) procedures for the Tekran measurements can be found in the Supplementary Information (SI).

During the two campaigns, meteorological parameters were measured using an automated weather station (Campbell Scientific Co., Ltd) including wind speed (WS, m s^{-1}), wind direction (WD, °), temperature (T, °C), surface pressure (P, kPa), relative humidity (RH, %), solar radiation (SR, W m^{-2}), and precipitation (PREC, mm). Fine particulate matter ($PM_{2.5}$) and sulfur dioxide (SO_2) concentrations were

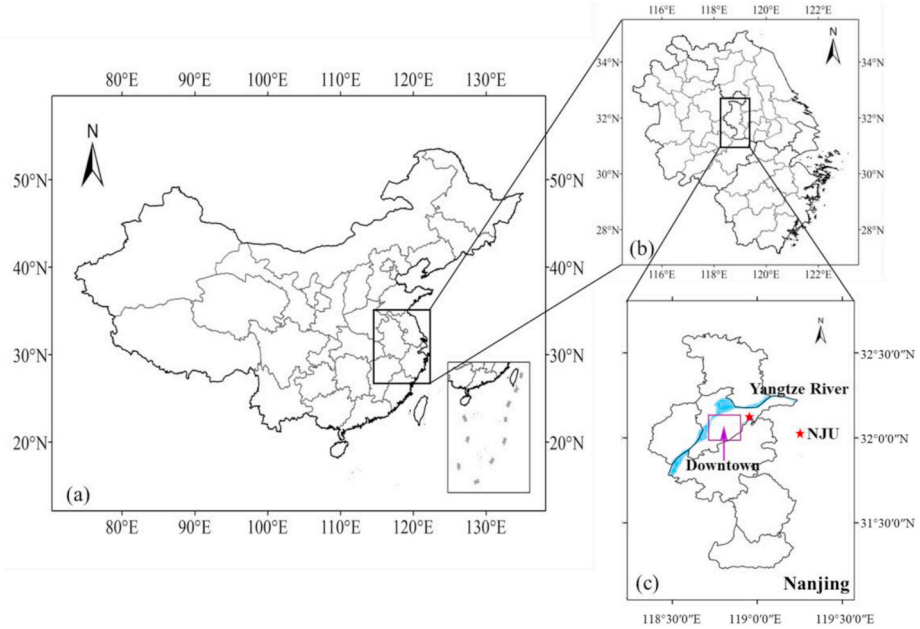

Fig. 1. The locations of (a) the Yangtze River Delta (YRD) region in China, (b) the city of Nanjing in the YRD region, and (c) the NJU site in Nanjing.

measured by Thermo Scientific TEOM 1405D and Model 43i SO_2 analyzer, respectively. In Campaign 2, particle size distribution ranging from 3 nm to 10 μm were measured by a wide-range particle spectrometer (Electrical Aerosol Spectrometry, Estonia). More details on the maintenance and calibration of the instruments used in this study are provided in the SI.

All the data of air pollutants and meteorological factors were hourly averaged for further analyses. Totally 3858 and 3774 valid GEM data were obtained in Campaigns 1 and 2, respectively.

2.3. Backward trajectory calculation and statistics

The Hybrid Single-Particle Lagrangian Integrated Trajectory (HYSPLIT) model v4.9 (Draxler and Hess, 1998) was used to compute 24-h air mass backward trajectories from NJU for every hour with the Global Data Assimilation System (GDAS) $1^\circ \times 1^\circ$ gridded meteorological data. The distance (DIS) and direction (DIR) of the endpoint of each 24-h trajectory from NJU were then calculated. The choice of the trajectory length can affect the performance of GAMs. The 24-h trajectories with the endpoints mostly within 600 km radius represent regional transport and were examined to yield the best GAM performance in this study. Moreover, the potential source contribution function (PSCF) model was utilized to identify the source regions of GEM in different seasons and two types of polluted episodes. To cover the source regions to a maximum extent, 72-h HYSPLIT backward trajectories with GDAS data for every 6 h were used for the PSCF model. The principle of the PSCF model is adapted from the study of Zhang et al. (2013). Details for HYSPLIT and PSCF can be found in the SI.

2.4. Description of GAMs

GAMs were adopted in this study to predict the GEM concentration. The "mgcv package" in the software R was used. The model can be described as follows:

$$g(\mu) = f_1(x_1) + f_2(x_2) + \cdots + f_k(x_k) + \varepsilon \quad (1)$$

where x_j ($j = 1, 2, \ldots, k$) are different meteorological predictors (e.g., WS, WD, T, P, RH, SR, PREC, DIS, DIR, etc.) with the corresponding f_j being the smooth functions of the predictors; ε is the residual; μ is the expected value of the response variable; and g is the link function which specifies the relationship between the non-linear formulation and the expected value (Gong et al., 2017; Wood, 2006).

The GEM concentration at NJU fits a skewed distribution. Therefore, the logarithm of GEM, which fits a Gaussian distribution, was selected as the response variable (see Figure S1). Accordingly, the model family and the link function were set to be Gaussian and the "identity" link in this study, respectively. Penalized cubic regression splines were used for the smooth functions.

Predictors for GAM were determined following the selecting procedure proposed by Gong et al. (2017) regarding the Akaike Information Criterion (AIC) and the R^2 values as the model performance. As predictors are added into the model, the AIC decreases and R^2 increases up to a point. The predictor candidates considered in this study include the following variables:

(1) Meteorological parameters measured at NJU: WS, WD, T, P, RH, SR, and PREC;
(2) Other meteorological parameters: boundary layer height (BLH), and total cloud cover (TCC) obtained from the European Centre for Medium-Range Weather Forecasts (ECMWF) reanalysis (https://www.ecmwf.int);
(3) HYSPLIT yields: DIS, and DIR;
(4) Other parameters: day of year (DOY).

Table S1 shows the changes of AIC and R^2 when new predictors were added to the model. WS, SR, T, RH, P, PREC, DIR, DIS, and DOY were chosen to be the final predictors, among which PREC was set to be a categorical predictor. There was no significant improvement of the model performance when WD, BLH, and TCC were added into the model. The model performance was examined using the gam. check function and the auto-correlation function in R. The gam. check function estimates the optimal degree of freedom for each predictor and generates the scatterplot of deviance residuals against theoretical quantiles (also known as the Q-Q plot), the scatterplot of residuals against linear predictor, the histogram of residuals, and the scatterplot of responses against fitted values. The auto-correlation function provides a useful tool to examine the autocorrelation of the model residuals. Results of model quality control are showed in Figure S2.

The time series of the "terms" of different predictors were obtained using the "predict by terms" function in R. The term of each predictor

denotes its impact on GEM, and is therefore named the impact of predictor (IOP). It should be noted that the IOP values could be both positive and negative because the intercept of the term for each predictor can not be obtained. Therefore, the absolute value of IOP is meaningless, but the variation of IOP is a useful tool for time series analysis in case studies.

3. Results and discussion

3.1. Seasonal variations of GEM in the two campaigns

The overall mean GEM concentrations (±standard deviation) at NJU in Campaigns 1 and 2 were 3.77 ± 1.32 ng m^{-3} and 3.24 ± 1.26 ng m^{-3}, respectively. The GEM level in the late campaign was about 2–2.5 times the background level (1.3–1.6 ng m^{-3}) of the Northern Hemisphere (Obrist et al., 2018; Sprovieri et al., 2016; Zhang et al., 2016), indicating significant contribution from anthropogenic Hg emissions. Fig. 2 shows the monthly variations of GEM concentration during the two campaigns. A significant decrease from Campaign 1 to Campaign 2 was found during summer and fall ($p < 0.05$) (summer: from 3.80 ± 1.07 ng m^{-3} to 2.85 ± 0.87 ng m^{-3}, fall: from 3.86 ± 1.27 ng m^{-3} to 3.28 ± 0.87 ng m^{-3}). The PSCF model was used to identify the potential source regions of GEM in different seasons in the two campaigns, as shown in Fig. 3. In the springtime of both campaigns, a polluted "belt" to the southwest of Nanjing tended to be the main source regions. A number of cement clinker producing facilities and non-ferrous metal smelters concentrated in the identified belt could be the major contributors of GEM in spring. The contribution of springtime source regions did not exhibit apparent alleviation from Campaign 1 to Campaign 2, which is consistent with the fact that GEM in April and May almost stayed at the same level between the two campaigns. On the contrary, the contribution of the summertime source region in Campaign 1 which was to the east of Nanjing, the more developed area in the YRD region, reduced evidently in Campaign 2, resulting in the significant drop of GEM in summer from Campaign 1 to Campaign 2. Long-range transport from the north turned out to be one crucial source of Hg pollution at NJU in fall and winter. As seen from Fig. 3, there are two main transport channels for the polluted air parcels from the North China Plain (NCP) region to NJU, one from the northwest (Channel 1) and the other from the northeast (Channel 2). In the fall of Campaign 1, air masses from the NCP region through the two channels and from the east made equivalent contributions to GEM pollution at NJU. The NCP contribution through Channel 2 decreased significantly in the fall of Campaign 2, leading to the big drop of GEM in September and October from Campaign 1 to Campaign 2. The wintertime NCP contribution alleviated through Channel 1 while strengthened through Channel 2 from Campaign 1 to Campaign 2. The air mass circulation to the south of the NJU site also contributed significantly to the accumulation of GEM pollution in the winter of Campaign 2.

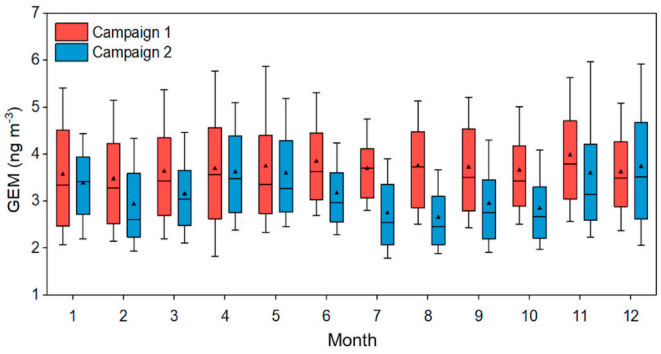

Fig. 2. Monthly variations of the observed gaseous elemental mercury (GEM) concentration at the NJU site in the two campaigns. The bottom and top of the box represent the 25th and 75th percentiles, respectively. The band inside the box represents the median value. The bottom and top ends of the whiskers represent the 10th and 90th percentiles. The triangle dot represents the mean value.

Results from PSCF models imply that the transport of Hg pollution could be the main cause of the change in seasonal patterns of GEM between the two campaigns.

3.2. Interpretation of overall results from GAMs

Fig. 4 shows the overall performance of GAMs for the two campaigns which is generally satisfactory with exceptions at high GEM concentrations. The adjusted R^2 values for Campaigns 1 and 2 are 0.43 and 0.57, respectively. GAMs were evaluated to be relatively robust when the adjusted R^2 values were over 0.5 (Gong et al., 2017; Wu et al., 2021). Therefore, based on the evaluation in previous studies and the case study (Section 3.3) in this study, the influencing patterns of predictors from the GAM for Campaign 2 were robust. Although the adjusted R^2 value of the GAM for Campaign 1 was a little lower than 0.5, the influencing patterns of predictors for Campaign 1 were similar as Campaign 2, and hence believed to be robust enough. The contributions of the eight predictors in the models were all significant ($p < 0.001$). The F test results from GAMs imply the variance contribution (i.e., the relative contribution) of each predictor to the response (Camalier et al., 2007; Gong et al., 2018). The yielded contributions of predictors from GAMs (the F value for each predictor divided by the sum of all F values) were shown in Fig. 5. RH and wind speed contributed nearly 60% of the variance of the dependent variable in Campaign 1, while RH, transport distance, and DOY were the three leading predictors in Campaign 2. From Campaign 1 to Campaign 2, the contribution of wind speed decreased significantly, and that of RH had a slight decrease. DOY and transport distance undertook more shares in Campaign 2. Meanwhile, the impacts of different predictors on GEM in Campaign 2 are revealed in Fig. 6 through scatterplots on the relationship between each predictor and their share of contribution in the logarithm of GEM yielded from the GAM model. Surface GEM concentration in urban or suburban areas can be considered as the sum of a regional background (the global or Northern Hemispheric background plus the contribution from long-range transport) and local signals (Alvarado et al., 2015). Impacts of local anthropogenic emissions, regional transport, and meteorological factors (including natural emissions) on GEM were estimated based on GAM results as discussed below.

3.2.1. Impacts of local anthropogenic emissions on GEM

Gong et al. (2017) found that the residuals from GAMs could indicate the impacts of wildfires on O_3 concentrations and this approach was verified by case study in different cities in the western US. In this study, the residuals from GAM could mainly stand for the contribution of local anthropogenic emissions. Modeled GEM at high levels tend to be underestimated for both campaigns, indicating that it could probably be under the influence of local anthropogenic emissions since local signals often generate spikes in GEM observations. To verify this hypothesis, two types of pollution episodes were identified in Campaign 2. Hours with the GEM concentration exceeding the campaign average were regarded as polluted hours, and a group of no less than eight consecutive polluted hours, plus 2 h before and 2 h after, was identified as a pollution episode (Zhang and Jaffe, 2017). A total of 70 GEM pollution episodes (3122 h) were ultimately identified in Campaign 2. Among these episodes, Episode A (n = 36) is defined to be those in which the absolute values of the residuals (observed GEM minus fitted GEM) are less than 0.2 ng m^{-3} for more than 70% of the time, i.e., with good model performance, while Episode B (n = 34) represents the remaining episodes which were not well captured by the GAM model.

Figure S3 shows the spatial distribution of the potential source regions for Episodes A and B using the PSCF model. Source regions for Episode B were concentrated within about 100 km radius of the NJU site, while sources for Episode A exhibited a regional pattern. Two typical examples of these two kinds of episodes with 72-h backward

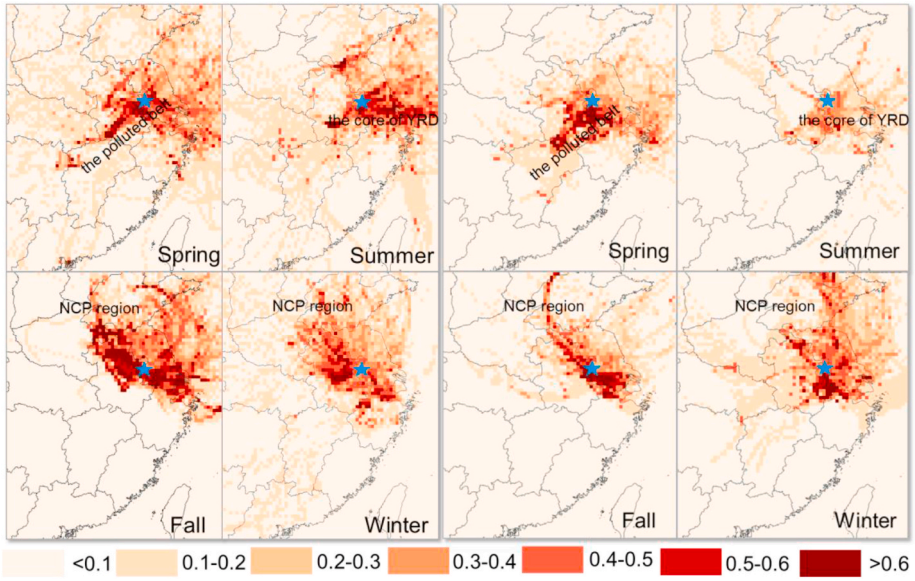

Fig. 3. Potential source regions of gaseous elemental mercury (GEM) in different seasons in two campaigns at NJU site based on the potential source contribution function (PSCF) model (left: Campaign 1; right: Campaign 2). Note that March to May is regarded as spring, June to August as summer, September to November as fall, and December to February as winter.

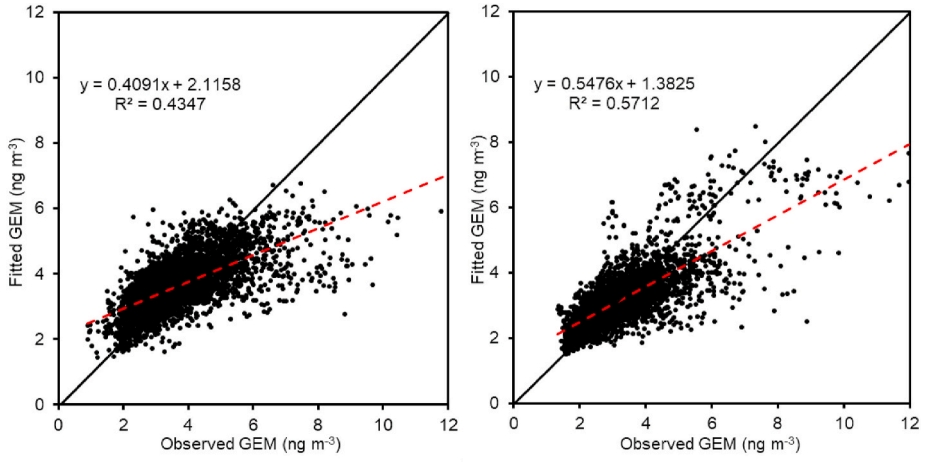

Fig. 4. Relationships between the observed and the fitted gaseous elemental mercury (GEM) concentrations in Campaign 1 (left) and Campaign 2 (right).

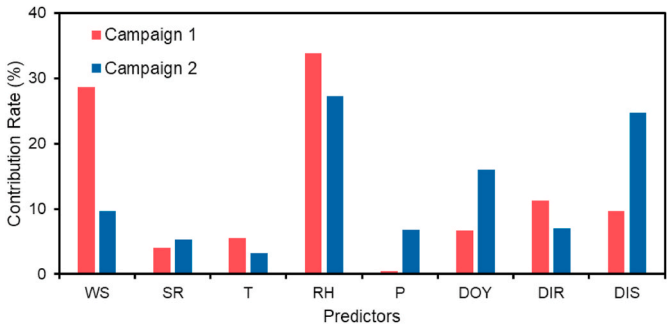

Fig. 5. Percentages of relative contribution from each predictor in the two campaigns (WS: wind speed; SR: solar radiation; T: temperature; RH: relative humidity; P: surface pressure; DOY: day of year; DIR: the direction of the endpoint of each 24-h trajectory; DIS: The distance of the endpoint of each 24-h trajectory).

trajectories are shown in Figure S4. The air masses in Episode A transported from the southwest to NJU through an ascending process to free troposphere followed by a fast descending process, indicating regional anthropogenic contribution. The air masses in Episode B, on the other hand, circulated around the NJU site and stayed at low elevations, implying the contribution from local anthropogenic sources. Therefore, the GAM model in this study reflected the regional background, including the East Asian background and the contribution from intra- and inter-regional anthropogenic sources, while the residuals represented the local anthropogenic emissions. The term "local" here could probably be defined as the area within about 100 km radius of the NJU site. The relative contribution of local emissions among different GEM sources is close to 1 minus the adjusted R^2 (i.e., the residual variance over the total variance). Therefore, the contribution of local anthropogenic emissions in the surrounding area of the NJU site decreased from over 50% to about 40% from Campaign 1 to Campaign 2. Figure S5 shows the extracted GEM time series for the two campaigns. The better performance of GAM for Campaign 2 than Campaign 1 implies the declining influence of local anthropogenic emissions at NJU. Monthly variations of the observed and the simulated GEM concentrations in the two campaigns are shown in Figure S6. The difference of the simulated

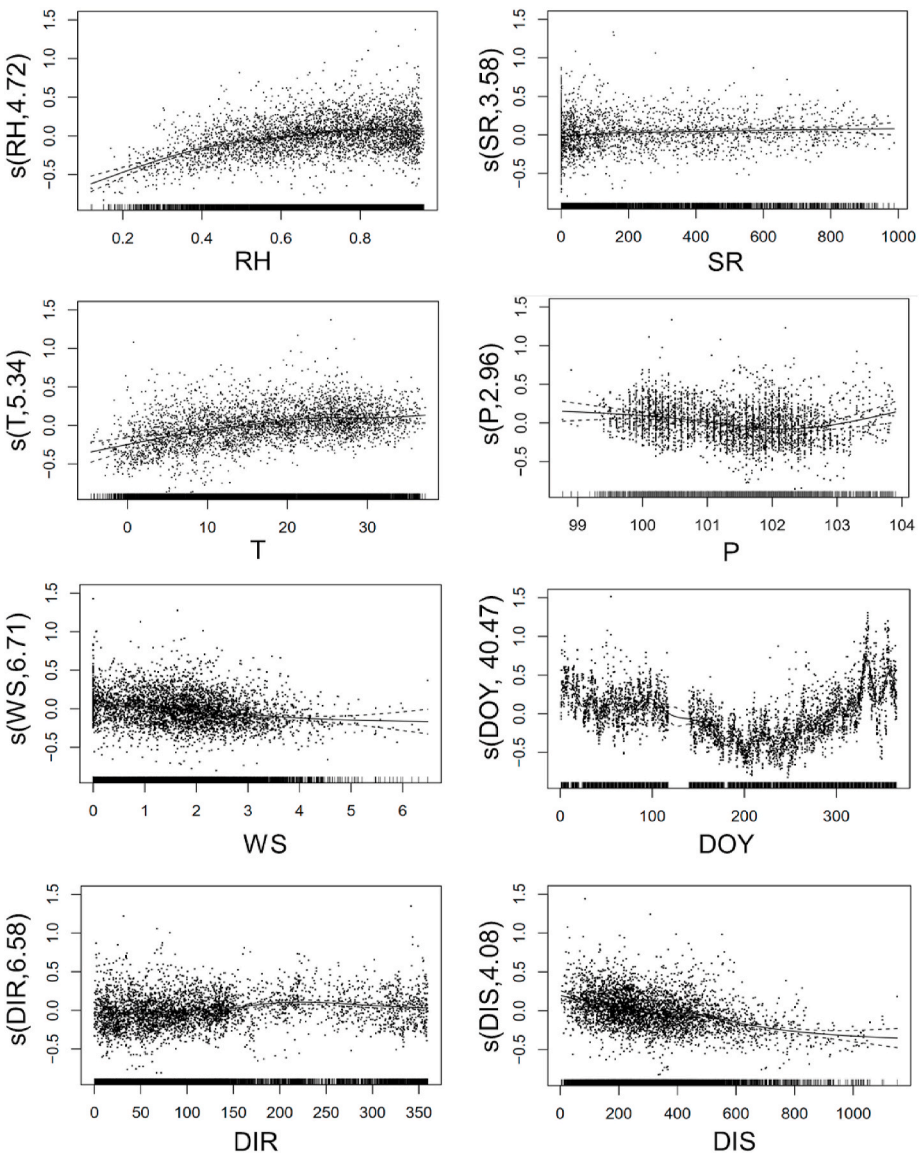

Fig. 6. Impacts of different predictors on the logarithm of gaseous elemental mercury (GEM) in the generalized additive model (GAM) for Campaign 2 (WS: wind speed; SR: solar radiation; T: temperature; RH: relative humidity; P: surface pressure; DOY: day of year; DIR: the direction of the endpoint of each 24-h trajectory; DIS: The distance of the endpoint of each 24-h trajectory; the y-axis in each subplot represents the smooth function term of each predictor with the corresponding degrees of freedom inside the brackets implying the impact of the predictor).

GEM between the two campaigns indicates the declining of regional background GEM, which was partially contributed by the reduction of regional anthropogenic emissions.

3.2.2. *Impacts of intra- and inter-regional transport on GEM*

Air parcel transport is divided into two types in this study, intra- and inter-regional transport. Intra-regional (or regional) transport denotes the transport within the YRD region, while inter-regional transport means transport from outside the YRD region to NJU. The two factors, direction and distance of the endpoints of backward trajectories, reveal the impacts of intra- and inter-regional transport (mostly within the YRD region) on GEM variation at NJU. As seen from Fig. 6, the main sources of GEM at NJU were from the east and the northeast (0–150°), which are the eastern and northern parts of the YRD region. However, air parcels from the southwest (~210°) had slightly higher GEM concentrations. This is consistent with the results from the PSCF model that the main source regions of GEM were from the area to the southwest of Nanjing in springtime. The partial response curve of transport distance showed that the major sources of GEM at NJU were concentrated within 600 km radius. GEM decreased with the transport distance, indicating that the regional Hg emission sources, especially those within 200 km radius had a much more significant impact on the GEM concentration than long-range transport. The decrease of the variance contribution of transport direction and the significant increase of variance contribution of transport distance from Campaign 1 to Campaign 2 suggested that the contribution of GEM from hotspot anthropogenic emission sources in the YRD region got mild.

GAM models with transport direction and distance for the endpoints of the 12-h backward trajectories (denoted as DIR/DIS-12 h) were also evaluated in this study. The R^2 values of GAMs for Campaigns 1 and 2 were 0.37 and 0.42, respectively, lower than those of GAMs with DIR/DIS-24 h (0.43 and 0.57). The discrepancy indicates that the 12-h backward trajectories were not able to cover the bulk source regions of Hg emissions for the site of NJU. Gong et al. (2017) found the 12-h backward trajectories slightly better than the 24-h backward trajectories in the GAM performance for 8 cities in the western US. The difference between this study and Gong et al. (2017) implies that regional transport of air pollution plays an important role at NJU and the near-surface transport feature in the YRD region limits the transport velocity. The comparison also suggests that transport direction and distance for the endpoints of backward trajectories should be applied to GAMs with caution and the transport time is a crucial parameter to be tested.

3.2.3. Impacts of meteorological factors on GEM

The influence of RH on the GEM concentration was prominent in both two campaigns. When RH was below 0.6, GEM increased rapidly with RH. When RH was higher than 0.6, the effect became mild. Given the influencing pattern, it was likely related to the Hg(II) reduction process in the aqueous phase of droplets and aerosols. When RH is low, the surface area of the air–water interface increases rapidly with the increase of RH, accelerating the reduction of Hg(II) (Subir et al., 2012). As RH reaches high level, the droplets and aerosols become larger and larger, resulting in mitigation of the surface area growth or precipitation both of which limit the increase of the Hg(II) reduction process (Deng et al., 2019; Lin et al., 2006; Subir et al., 2011). The SO_3^{2-} in the aqueous phase yielded from dissolved SO_2 can reduce Hg(II) and increase the GEM concentration (Lin et al., 2006; Subir et al., 2011). The mean PBM concentrations in Campaigns 1 and 2 (114 and 66 pg/m^3, respectively) were much higher than those at remote sites in China (Fu et al., 2015), which could provide more aqueous-phase environment for Hg(II) reduction. Further evidence with information on particle size distribution will be provided in Section 3.3 based on case study.

The reduction of Hg(II) is probably the reason for the subtle positive relationship between solar radiation and GEM as well. In aqueous phase, Hg is bound to inorganic, organic ligands or aquatic humic substances (Ariya et al., 2015). Light provides the energy required for the photolysis of the coordination compounds of Hg(II) via a ligand-to-metal charge transfer (LMCT) type of reaction. In this process, the ligand absorbs light energy and releases electrons to reduce Hg(II) to Hg(0). Meanwhile, light is also essential for the generation of reactive intermediates for Hg (II) reduction in some other photochemical reactions (Ariya et al., 2015). Therefore, solar radiation promotes the natural emissions of Hg, more specifically soil Hg emissions. However, due to the land use type (suburban landscaping) in the surrounding area of the NJU site, natural emissions had limited contribution to GEM enhancement. In addition, light also plays an important role in Hg(II) reduction in gaseous phase (Saiz-Lopez et al., 2018, 2019).

The partial response curve of air temperature in Fig. 6 shows that GEM increased with the rising of air temperature. The dependence of GEM on temperature has been observed in a number of previous studies (Sigler et al., 2009; Zhu et al., 2012; Yu et al., 2018). Zhu et al. (2012) found a positive correlation between temperature and the moving average TGM concentration at an urban site in eastern China in 2011, with a correlation coefficient of 0.43. They proposed that rising temperature promotes the emission of Hg from the soil. Pannu et al. (2014) used a quartz beaker system to examine the emission of Hg from both non-sterilized and sterilized soils with temperature increasing. They found that higher temperature not only stimulates the evasion of soil Hg (0), but also accelerates the microbiological Hg(II) reduction processes in soil. The impacts of both air temperature and solar radiation on GEM could be pointing to natural Hg emissions. However, according to the results of GAMs in this study, the contribution of air temperature and solar radiation to GEM was not as prominent as RH. Therefore, the crucial process that affects the GEM concentration level at suburban site like NJU could probably be the reduction process in the atmosphere instead of the evasion of soil Hg. Nevertheless, the contribution of air temperature could be somewhat underestimated because surface air pressure and air temperature had a significant negative correlation ($R = -0.844$, $p < 0.01$). Air pressure had a negative impact on GEM in the bulk variation range of 99–103 kPa, and part of the impact could be originated from air temperature. Although GAM allows the predictors to be not independent, strong correlation between predictors could still cause collinearity leading to inaccurate attribution.

A negative correlation was found between wind speed and GEM at the NJU site (Fig. 6). The wind speed observed at NJU in Campaign 2 was relatively low (<4 m s^{-1}). Lower wind speed leads to more stagnant meteorological condition which is unfavorable for GEM dispersion. Stronger winds enhance the local ventilation, resulting in the decrease of GEM (Belušić et al., 2015). Wind speed contributed nearly 30% of the variance in Campaign 1, but the contribution encountered an aggressive decline in Campaign 2 (Fig. 5), which was most likely due to the decrease of local signals at NJU. The alleviation of local anthropogenic emissions reduced the gradient of GEM between NJU and its surrounding clean areas, mitigating the impact of wind speed on GEM.

As an integrated predictor, DOY contains information on both the seasonal synoptic pattern and the climatic anomaly, representing the impacts of local meteorological control on air pollutants (Gong et al., 2018). The contribution of DOY to GEM was higher in winter and lower in summer for both campaigns. The air stagnation condition in winter caused more impacts from local meteorology in winter. From Campaign 1 to Campaign 2, with the decrease of the impact of local and regional anthropogenic Hg emissions, local meteorology tends to have greater impact on the variance of GEM. More discussion on the contribution of DOY will be found in Section 3.3.

PREC was a categorical predictor whose contribution can not be reflected in F values. PREC was found to have a negative relationship with GEM based on the time series of IOP, but the impact was very limited. This was possibly due to the scavenging of GOM and PBM by precipitation, resulting in a compensation of GEM converting to GOM and PBM. A case related to precipitation will be discussed in Section 3.3.4.

3.3. Interpretation of GAM results for case study

Each predictor played a unique role in affecting the GEM concentration in the two campaigns, although some predictors had larger effects than the others. The variation of GEM concentration was driven by perturbation of the predictors. Four types of cases were selected to analyze typical processes that have influence on GEM.

3.3.1. Case 1: Impacts of aqueous-phase Hg^{II} reduction on particles

RH was identified as the key meteorological factor for GEM in both campaigns at NJU. The impacts of RH were quasi-periodic on a daily basis and usually took place in the nighttime. Case 1 (April 15–16, 2019) was a typical event with GEM enhancement driven by the increase of RH. In this event, SO_2, $PM_{2.5}$ and particle size distribution were simultaneously monitored. The RH-driven GEM growth was from 10:00 on April 15 to 19:00 on April 16. As shown in Fig. 7c, there was a new particle formation (NPF) process starting at 10:00 on April 15 according to the results of particle size distribution (the "banana" pattern). The size of particles grew to 50–100 nm by approximately 21:00 with the increase of the $PM_{2.5}$ concentration (Fig. 7b). From midnight till the early morning of April 16, RH increased rapidly (Fig. 7b) while $PM_{2.5}$ decreased, indicating the hygroscopic growth and oversaturation of aerosol nuclei followed by the possible formation of fog droplets. Meanwhile, GEM increased gradually (Fig. 7a) and the IOP of RH exhibited significant enhancement (Fig. 7a). In view of the relatively high SO_2 level at NJU (Fig. 7b), the nighttime GEM enhancement was likely related to the reduction of Hg(II) in fog droplets by SO_3^{2-}. In the daytime of April 16, $PM_{2.5}$ experienced continuous increase. The rapid growth of RH from 12:00 to 18:00 probably accelerated the growth of $PM_{2.5}$ and augmented the condensed water on particles for the photoreduction of Hg(II), resulting in the rapid enhancement of GEM. Therefore, RH provided more aqueous environment for Hg(II) reduction, including the photolytic reduction process in the daytime and the SO_2-induced reduction at high SO_2 level. The decomposition of $HgSO_3$ in aqueous phase was neglected in recent modeling studies on the global scale (Horowitz et al., 2017). This case suggests that this reduction pathway might still have considerable contribution on a regional scale, especially in polluted cities in China.

3.3.2. Case 2: Impacts of regional transport

As discussed in Section 3.2.2, intra-regional transport has a much more significant impact on GEM than inter-regional transport at NJU. A typical event of long-range transport in the northeastern monsoon

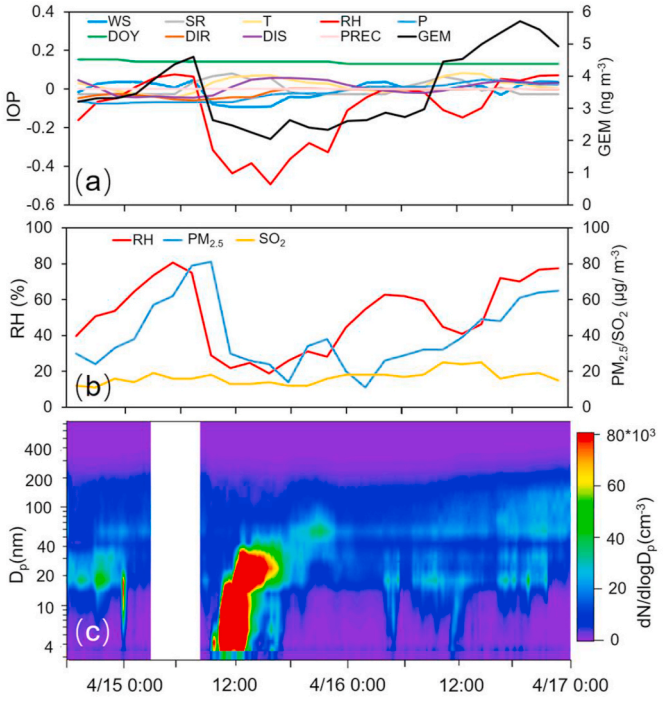

Fig. 7. Time series of (a) impacts of predictors (IOPs), the gaseous elemental mercury (GEM) concentration, (b) SO_2, $PM_{2.5}$, relative humidity, and (c) particle size distribution for Case 1 (WS: wind speed; SR: solar radiation; T: temperature; RH: relative humidity; P: surface pressure; DOY: day of year; DIR: the direction of the endpoint of each 24-h trajectory; DIS: The distance of the endpoint of each 24-h trajectory; PREC: precipitation).

season (November 17–19, 2018) was selected as Case 2. As shown in Fig. 8, the GEM concentration encountered gradual increase along with a sharp decrease of DIS-24 h and a fast deflection of DIR-24 h. The IOP of transport distance increased significantly. Based on 72-h backward trajectories (Figure S7), at the beginning of the event, the air masses originated from far north (Siberia) at a high elevation level, traveled through the circum-Bohai-sea region, and descended to NJU within a short period of time. The anthropogenic Hg emissions along this pathway were limited since it dodged both the NCP region and the core area of the YRD region. On the second day, the northeastern monsoon got mild, and the air masses started to pass through the more polluted region to the north of Nanjing at a lower velocity. The origin of the 72-h backward trajectories for the third day was within 200 km distance from NJU, indicating that the air masses circled around in the YRD region at a low wind speed and accumulated Hg pollution. There was a sharp increase in the IOP of transport direction on the evening of November 18, which suggests the impacts of sudden abatement of the northeastern monsoon. Most events of long-range transport were, like this event, accompanied by a descending process of air masses. Therefore, most of the time the air masses were relatively clean, making intra-regional transport a much larger contributor than inter-regional transport.

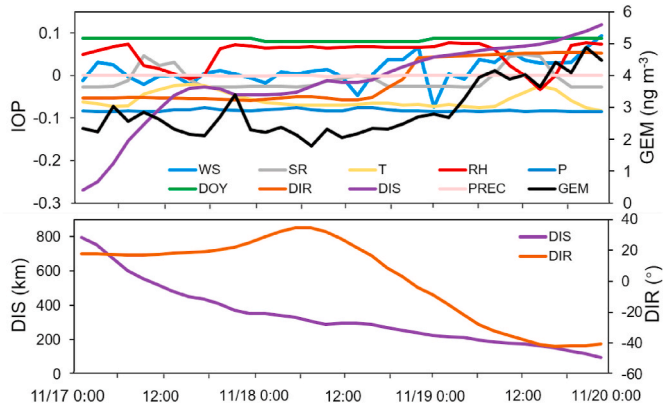

Fig. 8. Time series of (a) impacts of predictors (IOPs), the gaseous elemental mercury (GEM) concentration, and (b) distance and direction of the endpoint of the 24-h backward trajectory for Case 2 (WS: wind speed; SR: solar radiation; T: temperature; RH: relative humidity; P: surface pressure; DOY: day of year; DIR: the direction of the endpoint of each 24-h trajectory; DIS: The distance of the endpoint of each 24-h trajectory; PREC: precipitation).

3.3.3. *Case 3a and 3 b: Impacts of air stagnation*

Wind speed played an important role in Campaign 1 and took effect on a smaller temporal scale with frequent variation. The variation of the IOP of wind speed in a single event was not as prominent as RH, transport distance, or DOY, but the frequent perturbation of wind speed made it a key meteorological factor in Campaign 1. Figure S8 shows a typical episode with wind speed as the main driver of GEM enhancement, denoted as Case 3a (April 17–18, 2015). Wind speed decreased from 4 m s^{-1} to 1 m s^{-1} within 12 h in this episode, and meanwhile the GEM concentration almost doubled. The IOP of wind speed increased significantly in the episode. Stagnation weakened the diffusion process of air pollution, and consequently the concentration of GEM increased with Hg pollution accumulation. Generally, wind speed fluctuated rapidly and the impact of it on GEM was short and intermittent.

As a comprehensive predictor, DOY could be a proxy for other meteorological factors under certain circumstances. The impact of wintertime air stagnation in both campaigns was revealed by DOY. As seen in Fig. 9, the period of November 22 to December 10, 2018 (Case 3b) was a typical Hg pollution episode driven by the change of DOY. The enhancement of GEM was highly synchronized with the increase of the IOP of DOY. During this episode, about 70% of air masses were originated from the core area of the YRD region based on results from cluster analysis of 72-h backward trajectories (Figure S9). The relatively short transport distance indicated the stagnant atmospheric condition in the YRD region, which was verified by the low wind speed level (1.5 m s^{-1}). Air stagnation amplified the impact of regional anthropogenic emissions. Case 3b suggests that the variation of the IOP of DOY was on a much larger temporal scale than other meteorological factors.

3.3.4. *Case 4a and 4 b: Impacts of the 2015 El Niño episode*

The 2015–2016 El Niño event had been the third strongest El Niños since 1950. This El Niño event emerged in September 2014, and fully

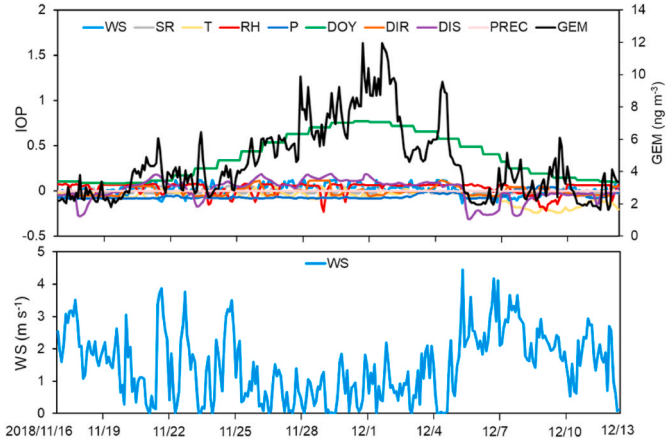

Fig. 9. Time series of (a) impacts of predictors (IOPs), the gaseous elemental mercury (GEM) concentration, and (b) wind speed for Case 3b (WS: wind speed; SR: solar radiation; T: temperature; RH: relative humidity; P: surface pressure; DOY: day of year; DIR: the direction of the endpoint of each 24-h trajectory; DIS: The distance of the endpoint of each 24-h trajectory; PREC: precipitation).

established in the spring of 2015. The overall impacts of the 2015 El Niño on meteorology in China were characterized by higher temperature, higher RH, and more precipitation (Zhai et al., 2016), which was mostly reflected by the predictor DOY in Campaign 1. Case 4 was also driven by the variation of DOY, but on a larger temporal scale than Case 3b.

As shown in Figure S10, DOY had a significantly larger impact on springtime GEM in Campaign 1 than in Campaign 2. As discussed in Section 3.2.3, both temperature and RH had positive impacts on GEM, probably through soil Hg(0) evasion and aqueous-phase Hg(II) reduction, respectively. Fig. 10 shows the time series of IOPs, GEM concentration, air temperature, and RH in a typical episode in spring 2015 (Case 4a). The impacts of air temperature and RH on GEM in spring 2015 were both reflected by the proxy predictor DOY on a larger temporal scale. This prolonged episode experienced an enhancement of temperature and a subsequent elevation of RH, both of which were captured by the increase of the IOP of DOY. The variations of impacts of air temperature and RH were less significant. The IOP of DOY reached the summit when RH attained the maximum level. However, the summit of GEM was more consistent with that of temperature than that of RH, indicating that temperature has a strong impact on GEM than RH in this case.

Temperature and RH were supposed to take effect on GEM in summer 2015 as well because of the El Niño event. However, the summertime GEM in Campaign 1 was not enhanced compared to Campaign 2. This was due to the offsetting effect of precipitation. There was much more precipitation in summer in Campaign 1 (1004 mm) than in Campaign 2 (191 mm). As discussed in Section 3.2.3, PREC had a negative impact on GEM. The impact of precipitation in summer 2015 were also embodied by the proxy predictor DOY on a larger temporal scale. As shown in Figure S11, with the significant increase of precipitation in Case 4b, the IOP of DOY was negatively strengthened, while the variation of the IOP of PREC was less significant.

4. Implications

Anthropogenic and natural perturbations, including changes in local anthropogenic emissions, regional transport, and meteorology (including natural emissions), all have impacts on GEM concentration in the ambient air. In this study, GAM was proved to be a promising tool in quantifying these impacts separately. Although the results from GAMs are semi-quantitative due to potential collinearity among certain predictors, the models can capture the interannual variation of contributions from different factors. The implications of the GAM results for the two campaigns are summarized as follows.

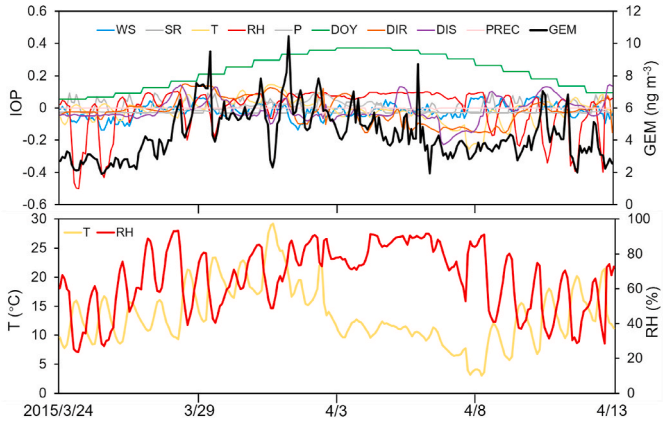

Fig. 10. Time series of (a) impacts of predictors (IOPs), the gaseous elemental mercury (GEM) concentration, (b) air temperature, and relative humidity for Case 4a (WS: wind speed; SR: solar radiation; T: temperature; RH: relative humidity; P: surface pressure; DOY: day of year; DIR: the direction of the endpoint of each 24-h trajectory; DIS: The distance of the endpoint of each 24-h trajectory; PREC: precipitation).

In Campaign 1, local anthropogenic emissions accounted for over 50% of the GEM variation according to the residuals from the GAM model. The processes of aqueous-phase Hg(II) reduction in droplets or particles and air stagnation played equivalently important roles in GEM enhancement which was indicated by the variance contributions and the IOPs of RH and wind speed, respectively. The contribution of regional transport to GEM was also pronounced in light of both PSCF results and the variance contributions of transport distance and direction. Based on the variation of the IOP of DOY in Campaign 1, the 2015 El Niño event had considerable impacts on GEM as well, especially the springtime GEM enhancement. Air temperature, RH, and precipitation all have stronger impacts in Campaign 1 than in Campaign 2 due to the El Niño.

In Campaign 2, the contribution of local anthropogenic emissions to GEM decreased significantly to about 40%. Correspondingly, the share of regional transport went up, which was revealed by the variance contributions of transport distance and direction. The variance contribution and IOP of DOY indicated that the wintertime air stagnation amplified the impacts of local and regional anthropogenic emissions. The pivotal meteorological factor was still RH in Campaign 2, suggesting the importance of the aqueous-phase Hg(II) reduction process.

From Campaign 1 to Campaign 2, the overall contribution of anthropogenic Hg emissions decreased, while the impacts of natural perturbations increased. With the implementation of the Minamata Convention on Mercury and the aggravation of global climate change, the impact ratio of natural perturbations over anthropogenic emissions will further increase. Therefore, long-term observations of Hg concentrations and data analyses with statistical tools like GAM are important procedures for policy making.

5. Conclusion

Two one-year-long campaigns were conducted at NJU, a suburban site in eastern China. The variation of the seasonal pattern of GEM indicated that GEM decreased significantly from Campaign 1 to Campaign 2 during summer and fall, which was mainly due to the change of Hg pollution source regions based on results from the PSCF model. GAM models were developed for the two campaigns respectively. GAMs had generally good performance with exceptions at high GEM concentrations since the impacts of local emissions were not considered in the models. The GAMs separated the local signals from the GEM concentration, which was verified by PSCF results. The decrease of residuals reflects the reduction of contribution from local anthropogenic emission sources.

The variance contribution of each predictor in GAMs was utilized to quantify the contribution of regional transport and meteorological factors. By incorporating the direction and distance of the endpoints of backward trajectories into GAMs, the Hg emissions within 200 km radius of NJU were found to play a more important role on the GEM concentration than long-range transport. The contribution from hotspot anthropogenic emission sources in the YRD region got mild between the two campaigns. Among all the meteorological factors, RH was found to have the most pronounced impact on GEM, followed by wind speed and DOY. Case studies provide more evidence of the impact mechanisms. The strong effect of RH was probably linked to Hg(II) reduction in the aqueous phase of droplets or particles in ambient air. Air stagnation exerted remarkable influence on GEM as well, which was revealed mainly by wind speed and partially by DOY in winter. The strong El Niño event in 2015 also had considerable impact on GEM through temperature, RH and precipitation.

CRediT authorship contribution statement

Lei Zhang: Conceptualization, Methodology, Writing - original draft, Writing - review & editing, Supervision, Funding acquisition. **Peisheng**

Zhou: Formal analysis, Investigation, Writing - original draft, Visualization. **Hui Zhong:** Investigation. **Yu Zhao:** Resources. **Liang Dai:** Investigation. **Qin'geng Wang:** Resources. **Mengxiao Xi:** Formal analysis. **Yi Lu:** Formal analysis. **Yutong Wang:** Formal analysis.

Declaration of competing interest

The authors declare that they have no known competing financial interests or personal relationships that could have appeared to influence the work reported in this paper.

Acknowledgment

This study was funded by the National Natural Science Foundation of China (No. 21876077) and the Fundamental Research Funds for the Central Universities in China (No. 14380080, No. 14380092, and No. 14380124).

Appendix A. Supplementary data

Supplementary data to this article can be found online at https://doi.org/10.1016/j.atmosenv.2020.118181.

References

Aldrin, M., Haff, I., 2005. Generalised additive modelling of air pollution, traffic volume and meteorology. Atmos. Environ. 39, 2145–2155.

Alvarado, M.L.C., Mountain, M., Hegarty, J., 2015. Investigating the impact of meteorology on O3 and PM2.5 trends, background levels, and NAAQS exceedances. TCEQ contract No. 582-15-50415. https://www.tceq.texas.gov/assets/public/implementation/air/am/contracts/reports/da/5821554118FY1501-20150831-aerMeteorologyAndO3PMTrends.pdf.

Amos, H.M., Jacob, D.J., Holmes, C.D., Fisher, J.A., Wang, Q., Yantosca, R.M., Corbitt, E. S., Galarneau, E., Rutter, A.P., Gustin, M.S., Steffen, A., Schauer, J.J., Graydon, J.A., Louis, V.L.S., Talbot, R.W., Edgerton, E.S., Zhang, Y., Sunderland, E.M., 2012. Gas-particle partitioning of atmospheric Hg(II) and its effect on global mercury deposition. Atmos. Chem. Phys. 12, 591–603.

Ariya, P.A., Amyot, M., Dastoor, A., Deeds, D., Feinberg, A., Kos, G., Poulain, A., Ryjkov, A., Semeniuk, K., Subir, M., Toyota, K., 2015. Mercury physicochemical and biogeochemical transformation in the atmosphere and at atmospheric interfaces: a review and future directions. Chem. Rev. 115, 3760–3802.

Belušić, A., Herceg-Bulić, I., Bencetić Klaić, Z., 2015. Using a generalized additive model to quantify the influence of local meteorology on air quality in Zagreb. Geofizika 32, 47–77.

Camalier, L., Cox, W., Dolwick, P., 2007. The effects of meteorology on ozone in urban areas and their use in assessing ozone trends. Atmos. Environ. 41, 7127–7137.

Choi, H.D., Huang, J., Mondal, S., Holsen, T.M., 2013. Variation in concentrations of three mercury (Hg) forms at a rural and a suburban site in New York State. Sci. Total Environ. 448, 96–106.

Cole, A.S., Steffen, A., Pfaffhuber, K.A., Berg, T., Pilote, M., Poissant, L., Tordon, R., Hung, H., 2013. Ten-year trends of atmospheric mercury in the high Arctic compared to Canadian sub-Arctic and mid-latitude sites. Atmos. Chem. Phys. 13, 1535–1545.

Deng, C., Tong, Y., Chen, L., Yuan, W., Sun, Y., Li, J., Wang, X., Zhang, W., Lin, H., Xie, H., Bu, X., 2019. Impact of particle chemical composition and water content on the photolytic reduction of particle-bound mercury. Atmos. Environ. 200, 24–33.

Ding, A.J., Fu, C.B., Yang, X.Q., Sun, J.N., Zheng, L.F., Xie, Y.N., Herrmann, E., Nie, W., Petäjä, T., Kerminen, V.M., Kulmala, M., 2013. Ozone and fine particle in the western Yangtze River Delta: an overview of 1 yr data at the SORPES station. Atmos. Chem. Phys. 13, 5813–5830.

Draxler, R.R., Hess, G.D., 1998. An overview of the HYSPLIT_4 modelling system for trajectories, dispersion and deposition. Aust. Meteorol. Mag. 47, 295–308.

Driscoll, C.T., Mason, R.P., Chan, H.M., Jacob, D.J., Pirrone, N., 2013. Mercury as a global pollutant: sources, pathways, and effects. Environ. Sci. Technol. 47, 4967–4983.

Fu, X.W., Zhang, H., Yu, B., Wang, X., Lin, C.J., Feng, X.B., 2015. Observations of atmospheric mercury in China: a critical review. Atmos. Chem. Phys. 15, 9455–9476.

Giang, A., Selin, N.E., 2016. Benefits of mercury controls for the United States. Proc. Natl. Acad. Sci. U.S.A. 113, 286–291.

Gong, X., Hong, S., Jaffe, D.A., 2018. Ozone in China: spatial distribution and leading meteorological factors controlling O3 in 16 Chinese cities. Aerosol Air Qual. Res. 18, 2287–2300.

Gong, X., Kaulfus, A., Nair, U., Jaffe, D.A., 2017. Quantifying O3 impacts in urban areas due to wildfires using a generalized additive model. Environ. Sci. Technol. 51, 13216–13223.

Gustin, M.S., Amos, H.M., Huang, J., Miller, M.B., Heidecorn, K., 2015. Measuring and modeling mercury in the atmosphere: a critical review. Atmos. Chem. Phys. 15, 5697–5713.

Hong, Q., Xie, Z., Liu, C., Wang, F., Xie, P., Kang, H., Xu, J., Wang, J., Wu, F., He, P., Mou, F., Fan, S., Dong, Y., Zhan, H., Yu, X., Chi, X., Liu, J., 2016. Speciated atmospheric mercury on haze and non-haze days in an inland city in China. Atmos. Chem. Phys. 16, 13807–13821.

Horowitz, H.M., Jacob, D.J., Zhang, Y., Dibble, T.S., Slemr, F., Amos, H.M., Schmidt, J. A., Corbitt, E.S., Marais, E.A., Sunderland, E.M., 2017. A new mechanism for atmospheric mercury redox chemistry: implications for the global mercury budget. Atmos. Chem. Phys. 17, 6353–6371.

Landis, M.S., Stevens, R.K., Schaedlich, F., Prestbo, E.M., 2002. Development and characterization of an annular denuder methodology for the measurement of divalent inorganic reactive gaseous mercury in ambient air. Environ. Sci. Technol. 36, 3000–3009.

Lin, C.-J., Pongprueksa, P., Lindberg, S.E., Pehkonen, S.O., Byun, D., Jang, C., 2006. Scientific uncertainties in atmospheric mercury models I: model science evaluation. Atmos. Environ. 40, 2911–2928.

Liu, K., Wang, S., Wu, Q., Wang, L., Ma, Q., Zhang, L., Li, G., Tian, H., Duan, L., Hao, J., 2018. A highly resolved mercury emission inventory of Chinese coal-fired power plants. Environ. Sci. Technol. 52, 2400–2408.

Liu, K., Wu, Q., Wang, L., Wang, S., Liu, T., Ding, D., Tang, Y., Li, G., Tian, H., Duan, L., Wang, X., Fu, X., Feng, X., Hao, J., 2019. Measure-specific effectiveness of air pollution control on China's atmospheric mercury concentration and deposition during 2013-2017. Environ. Sci. Technol. 53, 8938–8946.

Nair, U.S., Wu, Y., Walters, J., Jansen, J., Edgerton, E.S., 2012. Diurnal and seasonal variation of mercury species at coastal-suburban, urban, and rural sites in the southeastern United States. Atmos. Environ. 47, 499–508.

Nguyen, L.S.P., Sheu, G.R., Lin, D.W., Lin, N.H., 2019. Temporal changes in atmospheric mercury concentrations at a background mountain site downwind of the East Asia continent in 2006-2016. Sci. Total Environ. 686, 1049–1056.

Obrist, D., Kirk, J.L., Zhang, L., Sunderland, E.M., Jiskra, M., Selin, N.E., 2018. A review of global environmental mercury processes in response to human and natural perturbations: changes of emissions, climate, and land use. Ambio 47, 116–140.

Pacyna, J.M., Travnikov, O., De Simone, F., Hedgecock, I.M., Sundseth, K., Pacyna, E.G., Steenhuisen, F., Pirrone, N., Munthe, J., Kindbom, K., 2016. Current and future levels of mercury atmospheric pollution on a global scale. Atmos. Chem. Phys. 16, 12495–12511.

Pannu, R., Siciliano, S.D., O'Driscoll, N.J., 2014. Quantifying the effects of soil temperature, moisture and sterilization on elemental mercury formation in boreal soils. Environ. Pollut. 193, 138–146.

Pearce, J.L., Beringer, J., Nicholls, N., Hyndman, R.J., Tapper, N.J., 2011. Quantifying the influence of local meteorology on air quality using generalized additive models. Atmos. Environ. 45, 1328–1336.

Qin, X., Wang, X., Shi, Y., Yu, G., Zhao, N., Lin, Y., Fu, Q., Wang, D., Xie, Z., Deng, C., Huang, K., 2019. Characteristics of atmospheric mercury in a suburban area of east China: sources, formation mechanisms, and regional transport. Atmos. Chem. Phys. 19, 5923–5940.

Rutterford, L.A., Simpson, S.D., Jennings, S., Johnson, M.P., Blanchard, J.L., Schön, P.-J., Sims, D.W., Tinker, J., Genner, M.J., 2015. Future fish distributions constrained by depth in warming seas. Nat. Clim. Change 5, 569–573.

Saiz-Lopez, A., Acuna, A.U., Trabelsi, T., Carmona-Garcia, J., Davalos, J.Z., Rivero, D., Cuevas, C.A., Kinnison, D.E., Sitkiewicz, S.P., Roca-Sanjuan, D., Francisco, J.S., 2019. Gas-phase photolysis of Hg(I) radical species: a new atmospheric mercury reduction process. J. Am. Chem. Soc. 141, 8698–8702.

Saiz-Lopez, A., Sitkiewicz, S.P., Roca-Sanjuan, D., Oliva-Enrich, J.M., Davalos, J.Z., Notario, R., Jiskra, M., Xu, Y., Wang, F., Thackray, C.P., Sunderland, E.M., Jacob, D. J., Travnikov, O., Cuevas, C.A., Acuna, A.U., Rivero, D., Plane, J.M.C., Kinnison, D. E., Sonke, J.E., 2018. Photoreduction of gaseous oxidized mercury changes global atmospheric mercury speciation, transport and deposition. Nat. Commun. 9, 4796.

Schroeder, W.H., Munthe, J., 1998. Atmospheric mercury - an overview. Atmos. Environ. 32, 809–822.

Selin, H., Keane, S.E., Wang, S., Selin, N.E., Davis, K., Bally, D., 2018. Linking science and policy to support the implementation of the Minamata Convention on Mercury. Ambio 47, 198–215.

Sigler, J.M., Mao, H., Talbot, R., 2009. Gaseous elemental and reactive mercury in Southern New Hampshire. Atmos. Chem. Phys. 9, 1929–1942.

Slemr, F., Brunke, E.G., Ebinghaus, R., Kuss, J., 2011. Worldwide trend of atmospheric mercury since 1995. Atmos. Chem. Phys. 11, 4779–4787.

Slemr, F., Brunke, E.G., Labuschagne, C., Ebinghaus, R., 2008. Total gaseous mercury concentrations at the Cape Point GAW station and their seasonality. Geophys. Res. Lett. 35.

Sprovieri, F., Pirrone, N., Bencardino, M., D'Amore, F., Carbone, F., Cinnirella, S., Mannarino, V., Landis, M., Ebinghaus, R., Weigelt, A., Brunke, E.G., Labuschagne, C., Martin, L., Munthe, J., Wangberg, I., Artaxo, P., Morais, F., de Melo Jorge Barbosa, H., Brito, J., Cairns, W., Barbante, C., Del Carmen Dieguez, M., Garcia, P.E., Dommergue, A., Angot, H., Magand, O., Skov, H., Horvat, M., Kotnik, J., Read, K.A., Neves, L.M., Gawlik, B.M., Sena, F., Mashyanov, N., Obolkin, V., Wip, D., Feng, X.B., Zhang, H., Fu, X., Ramachandran, R., Cossa, D., Knoery, J., Marusczak, N., Nerentorp, M., Norstrom, C., 2016. Atmospheric mercury concentrations observed at ground-based monitoring sites globally distributed in the framework of the GMOS network. Atmos. Chem. Phys. 16, 11915–11935.

Streets, D.G., Horowitz, H.M., Lu, Z., Levin, L., Thackray, C.P., Sunderland, E.M., 2019. Global and regional trends in mercury emissions and concentrations. 2010–2015. Atmos. Environ. 201, 417–427.

Subir, M., Ariya, P.A., Dastoor, A.P., 2011. A review of uncertainties in atmospheric modeling of mercury chemistry I. Uncertainties in existing kinetic parameters – Fundamental limitations and the importance of heterogeneous chemistry. Atmos. Environ. 45, 5664–5676.

Subir, M., Ariya, P.A., Dastoor, A.P., 2012. A review of the sources of uncertainties in atmospheric mercury modeling II. Mercury surface and heterogeneous chemistry – a missing link. Atmos. Environ. 46, 1–10.

Tang, Y., Wang, S., Wu, Q., Liu, K., Wang, L., Li, S., Gao, W., Zhang, L., Zheng, H., Li, Z., Hao, J., 2018. Recent decrease trend of atmospheric mercury concentrations in East China: the influence of anthropogenic emissions. Atmos. Chem. Phys. 18, 8279–8291.

Un Environment, 2019. Global Mercury Assessment 2018. UN Environment Programme. Chemicals and Health Branch Geneva, Switzerland.

Weigelt, A., Ebinghaus, R., Manning, A.J., Derwent, R.G., Simmonds, P.G., Spain, T.G., Jennings, S.G., Slemr, F., 2015. Analysis and interpretation of 18 years of mercury observations since 1996 at Mace Head, Ireland. Atmos. Environ. 100, 85–93.

Weiss-Penzias, P.S., Gay, D.A., Brigham, M.E., Parsons, M.T., Gustin, M.S., Ter Schure, A., 2016. Trends in mercury wet deposition and mercury air concentrations across the U.S. and Canada. Sci. Total Environ. 568, 546–556.

Wood, S., 2006. Generalized Additive Models: an Introduction with R. Chapman and Hall/CRC, Boca Raton.

Wood, S.N., Augustin, N.H., 2002. GAMs with integrated model selection using penalized regression splines and applications to environmental modelling. Ecol. Model. 157, 157–177.

Wu, Q., Wang, S., Li, G., Liang, S., Lin, C.J., Wang, Y., Cai, S., Liu, K., Hao, J., 2016. Temporal trend and spatial distribution of speciated atmospheric mercury emissions in China during 1978-2014. Environ. Sci. Technol. 50, 13428–13435.

Wu, Q., Wang, S., Liu, K., Li, G., Hao, J., 2018. Emission-limit-oriented strategy to control atmospheric mercury emissions in coal-fired power plants toward the implementation of the Minamata convention. Environ. Sci. Technol. 52, 11087–11093.

Wu, Q., Tang, Y., Wang, L., Wang, S., Han, D., Ouyang, D., Jiang, Y., Xu, P., Xue, Z., Hu, J., 2021. Impact of emission reductions and meteorology changes on atmospheric mercury concentrations during the COVID-19 lockdown. Sci. Total Environ. 750, 142323.

Yu, Q., Luo, Y., Wang, S., Wang, Z., Hao, J., Duan, L., 2018. Gaseous elemental mercury (GEM) fluxes over canopy of two typical subtropical forests in south China. Atmos. Chem. Phys. 18, 495–509.

Zhai, P., Yu, R., Guo, Y., Li, Q., Ren, X., Wang, Y., Xu, W., Liu, Y., Ding, Y., 2016. The strong El Niño in 2015/2016 and its dominant impacts on global and China's climate. Acta Meteorol. Sin. 74, 309–321.

Zhang, L., Jaffe, D.A., 2017. Trends and sources of ozone and sub-micron aerosols at the Mt. Bachelor Observatory (MBO) during 2004–2015. Atmos. Environ. 165, 143–154.

Zhang, L., Lyman, S., Mao, H., Lin, C.-J., Gay, D.A., Wang, S., Sexauer Gustin, M., Feng, X., Wania, F., 2017a. A synthesis of research needs for improving the understanding of atmospheric mercury cycling. Atmos. Chem. Phys. 17, 9133–9144.

Zhang, L., Wang, L., Wang, S., Dou, H., Li, J., Li, S., Hao, J., 2017b. Characteristics and sources of speciated atmospheric mercury at a coastal site in the east China sea region. Aerosol Air Qual. Res. 17, 2913–2923.

Zhang, L., Wang, S., Wang, L., Wu, Y., Duan, L., Wu, Q., Wang, F., Yang, M., Yang, H., Hao, J., Liu, X., 2015. Updated emission inventories for speciated atmospheric mercury from anthropogenic sources in China. Environ. Sci. Technol. 49, 3185–3194.

Zhang, L., Wang, S.X., Wang, L., Hao, J.M., 2013. Atmospheric mercury concentration and chemical speciation at a rural site in Beijing, China: implication of mercury emission sources. Atmos. Chem. Phys. 13, 10505–10516.

Zhang, L., Wright, L.P., Blanchard, P., 2009. A review of current knowledge concerning dry deposition of atmospheric mercury. Atmos. Environ. 43, 5853–5864.

Zhang, Y., Jacob, D.J., Horowitz, H.M., Chen, L., Amos, H.M., Krabbenhoft, D.P., Slemr, F., St Louis, V.L., Sunderland, E.M., 2016. Observed decrease in atmospheric mercury explained by global decline in anthropogenic emissions. Proc. Natl. Acad. Sci. U.S.A. 113, 526–531.

Zhao, Y., Zhong, H., Zhang, J., Nielsen, C.P., 2015. Evaluating the effects of China's pollution controls on inter-annual trends and uncertainties of atmospheric mercury emissions. Atmos. Chem. Phys. 15, 4317–4337.

Zhu, J., Wang, T., Bieser, J., Matthias, V., 2015. Source attribution and process analysis for atmospheric mercury in eastern China simulated by CMAQ-Hg. Atmos. Chem. Phys. 15, 8767–8779.

Zhu, J., Wang, T., Talbot, R., Mao, H., Hall, C.B., Yang, X., Fu, C., Zhuang, B., Li, S., Han, Y., Huang, X., 2012. Characteristics of atmospheric total gaseous mercury (TGM) observed in urban nanjing, China. Atmos. Chem. Phys. 12, 12103–12118.